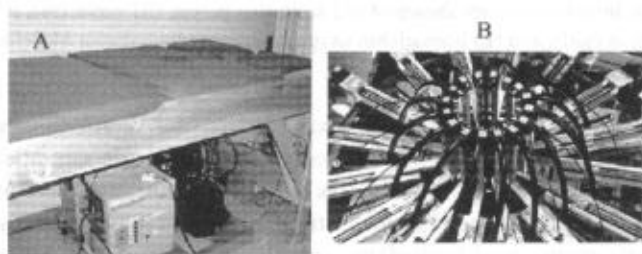**FIGURE 21.11** Hemoglobin saturation vs. total hemoglobin concentration; the dashed lines indicate the ranges for normal tissue from the mean and standard deviation of the healthy breast tissue.


FIGURE 21.12 (A) Patient bed for the optical breast imaging system developed at Dartmouth. (B) The fiber optic array for coupling light to and from the patient. The larger black cables are the detector fibers. The fibers are mounted on posts that translate radially for making contact with the tissue.

and, importantly, indicates the range of values that malignant tumors must have to be clearly distinguishable from the typical variation of normal breast tissue.

21.4.2.2 Clinical Optical Images of Breast Lesions

The optical breast imaging system developed by the group at Dartmouth is shown in Figure 21.12.[15,191] It is a pendant system, similar in many respects to the one at the University of Pennsylvania, but it obtains a coronal image of one breast at a time with a ring of interspersed 16 source and 16 detector fibers. The fiber ring is vertically positioned by a translation stage to image different planes of interest. The laser diodes emit light at 761, 785, 808, and 826 nm, are modulated at 100 MHz, and are optically combined before being serially multiplexed to each of the 16 source fibers. The lasers are driven sequentially so that the signal at each of the 16 photodetectors distinguishes different wavelengths and positions by time-division multiplexing. At each of the 4 wavelengths, 256 independent measurements are obtained and then processed by a finite element program to reconstruct absorption and scattering images (as described in Pogue et al.[15] and McBride et al.[191]).

Figure 21.13 shows optical images for a 73-year-old female volunteer who had undergone routine mammography that demonstrated a 2.5-cm focal density with a larger ~6-cm-diameter area of associated architectural distortion. The imaged lesion corresponded to a palpable mass; needle biopsy subsequently diagnosed the mass as an invasive ductal carcinoma. The optical image was acquired 2 weeks after the biopsy and was aligned such that the coronal imaging plane was centered on the palpable lump. From
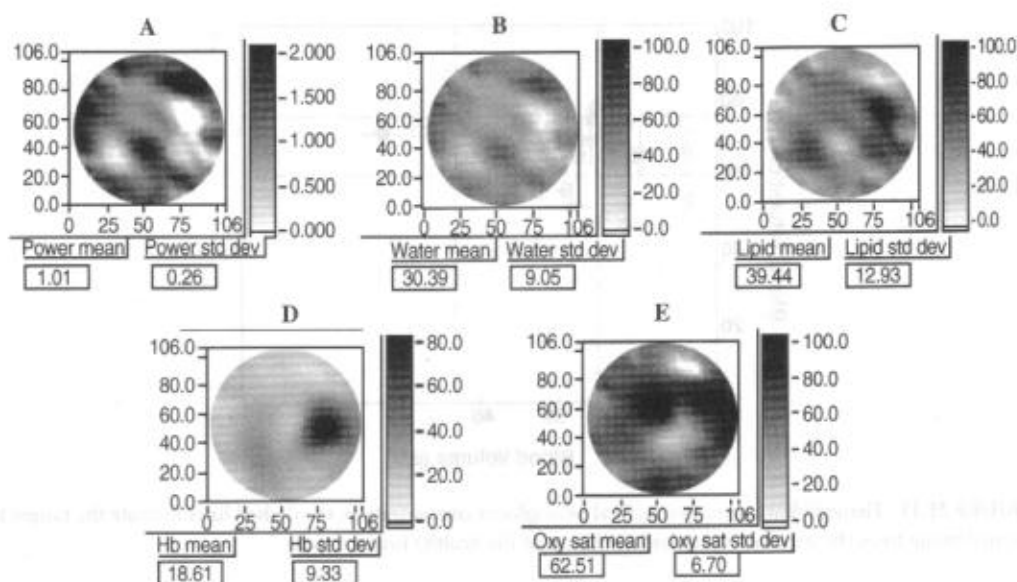
FIGURE 21.13 Clinical breast images are shown of (A) scattering power, (B) water (%), (C) lipids (%), (D) total hemoglobin concentration (μM), and (E) hemoglobin oxygen saturation (%). (From McBride, T.O. et al., *J. Biomed. Opt.*, 7, 72, 2002. With permission.)

the scattering and absorption information, images were derived of the scatter power,[191,227] water concentration, lipid concentration, total hemoglobin concentration, and oxygen saturation. A lesion is clearly visible in the total hemoglobin image, which shows a threefold contrast-to-background ratio. In comparison to the variation of total hemoglobin concentration observed in normal tissue (Figure 21.11), the tumor has significantly greater total hemoglobin concentration. Structures in the other physiological images do not correspond well to the hemoglobin image; however, sensitivity to water and lipid percentages is expected to be weak because of the chosen wavelengths. The similarity between the scattering power, water, and lipid images suggests that water and lipid images are susceptible to crosstalk from the scattering power image.

### 21.4.2.3　Contrast Agents to Enhance Breast Lesion Detection

Another experiment at the University of Pennsylvania employed a time-domain imaging system in transmission mode to acquire *contrast enhanced* breast images while simultaneously obtaining magnetic resonance images. The time-domain optical imager has been described in detail in References 13 and 228. The instrument uses time-correlated single photon counting to measure the TPSF of photons diffusing through the breast tissue. The TPSF is then Fourier transformed to produce data at multiple modulation frequencies, which are then used to reconstruct differential absorption images[188] of the contrast agent ICG. The 830-nm pulsed laser source is coupled to 24 source fibers through a fiber optic switch. The detection collects light from eight positions simultaneously. Thus images are obtained using 24 × 8 measurements times the number of modulation frequencies. All source fibers are mounted on one plate forming a 3 × 8 array of fibers spaced by intervals of 1.25 cm. The detector fibers are mounted on the other plate to form a 2 × 4 array with a 2.5-cm separation. These two plates stabilize the breast and also contain the RF coils for the MRI. The MR studies were performed with a 1.5 T Signa, GE Medical Systems imager.

Figure 21.14 shows the results from a 70-year-old patient with an infiltrating ductal carcinoma about 1 cm in diameter. The pre-gadolinium (Gd) enhanced sagittal MR image slice passing through the carcinoma is shown in Figure 21.14A in gray scale, while the relative signal increase due to the Gd is
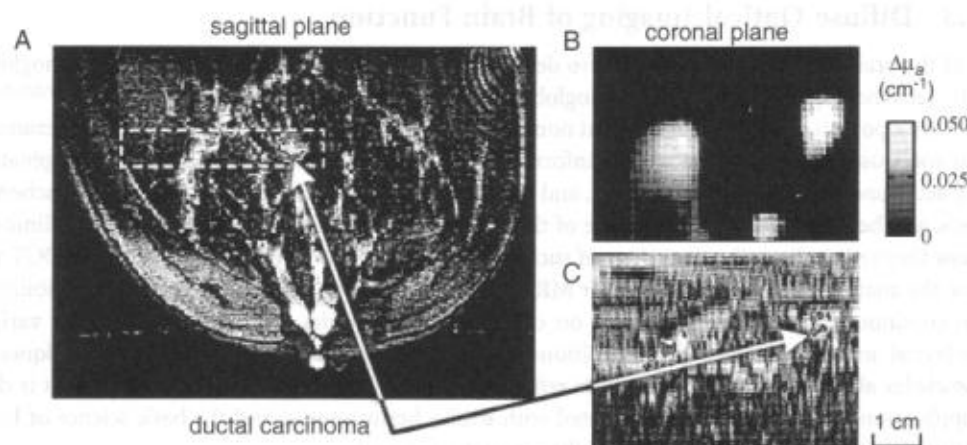
FIGURE 21.14 (Color figure follows p. 28-30.) A dynamic MRI and contrast-enhanced DOT image of a ductal carcinoma. (A) A dynamic sagittal MR image after Gd contrast enhancement passing through the center of the malignant lesion. (B) The coronal DOT image, perpendicular to the plane of the MRI image in (A), but in the volume of interest indicated in (A) by the dashed-line box. (C) The dynamic MR coronal image resliced from the same volume of interest and same dimensions as (B).

shown in color. A rectangle surrounding the carcinoma indicates the sagittal cut of the region of interest that was reconstructed in the optical image (shown in Figure 21.14B) in the coronal plane, and the corresponding MR coronal slice shown in Figure 21.14C. A strong optical contrast-induced absorption increase is seen in the upper right of the optical image, congruent with the position of the carcinoma revealed in the coronal MR image. Another lesion is revealed in the left of the optical image, congruent with the Gd enhancement observed in the MR image, but with a different size and shape. The differences in size and shape can be explained by the low spatial resolution of this implementation of DOT and the chosen threshold level for displaying the images. Similar results were seen in other patients with malignant and benign lesions. A summary of tissue ICG absorption enhancement seen in a group of patients is shown in Figure 21.15. This summary suggests that malignant lesions enhance absorption more than benign lesions by a factor of two, and more than normal tissue by a factor of three to four.
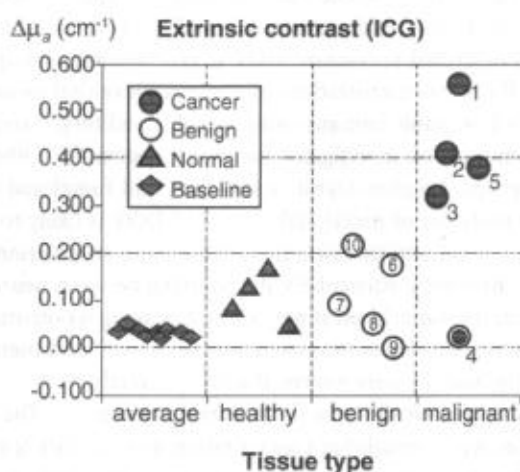
FIGURE 21.15 The ICG-induced absorption enhancement in healthy tissue and benign and malignant lesions compared with the nonenhanced absorption coefficient of normal healthy tissue.

21.4.3 Diffuse Optical Imaging of Brain Function

DOT of the brain affords continuous, *in vivo* deep tissue[161,229] measurements of cerebral oxyhemoglobin (HbO), deoxyhemoglobin (Hb), total hemoglobin (HbT = HbO + Hb), and even blood flow.[197,230–232] It is therefore a potentially new and important noninvasive technique for bedside monitoring. For example, optical spectroscopy can provide crucial information about cerebral hemodynamics and oxygenation during acute and chronic brain conditions, and optical imaging enables the detection of brain ischemia, necrosis, and hemorrhage.[233,234] Knowledge of the most appropriate optical parameters to use clinically, and how they reflect the pathophysiology of such conditions, is still evolving. It is unlikely that DOT will achieve the anatomical resolution of CT or MRI, but its noninvasive nature, low cost, and capability to obtain continuous, real-time information on cerebral hemodynamics and oxygenation under various physiological and pathophysiological conditions constitute a major advantage over other techniques.

Knowledge about how optical parameters reflect tissue pathophysiology is still evolving, but it is clear that application areas for DOT are associated with stroke, brain trauma, and the basic science of brain activation. We elaborate briefly on each of these target areas next.

Diffuse optical tomography offers an attractive alternative for diagnosing and monitoring internal bleeding and ischemic stroke when CT and MRI are not available. There are several possible optical signal indications of stroke. Using a bolus of intravascular contrast agent, it is possible to monitor mean cortical transit times; transit time changes there can reveal flow variations associated with ischemic stroke. Quantitative differential spectroscopy can indicate alterations in hemoglobin saturation in affected tissue due to reduced perfusion or modulated metabolic demand. Bleeding stroke can also be detected spectroscopically, in this case via a large blood volume increase. Scattering contrasts are also possible. Edema and swelling may provide heterogeneities in images of tissue scattering.

The feasibility of near-infrared spectroscopy (NIRS) to detect brain hemorrhage in patients with head trauma has been demonstrated.[27] Studies that compare primitive diffuse optical measurements of brain hematomas with CT images clearly demonstrate a correlation between the optical signal and hematoma location.[26,27,235] These correlation studies have shown that subcortical hemorrhages as deep as 3 cm beneath the cortical surface and as small as 5 mm in diameter can be detected. Furthermore, the different classes of hemorrhages give characteristically different signals. These pilot NIRS results are promising, but they are based on simple relative NIRS measures. Quantitative images of hemoglobin saturation and fast hemodynamics will provide great improvement in available diagnostic information over the data involved in these pilot studies. A means to detect early hemorrhage in at-risk patients — i.e., those treated with thrombolysis or anticoagulants — would have tremendous value. In addition, swelling and edema may be detectable through alterations in the scattering coefficient of the tissue.

Beyond the clinical uses described previously, DOT is experiencing widespread application in functional brain imaging. Since the first demonstrations of noninvasive optical measures of brain function,[29–31] studies have been performed on adult humans using visual,[32] auditory,[33] and somatosensory stimuli.[34] In addition, a number of studies have investigated the motor system.[35–37] Other areas of scientific investigation have included language,[38] higher cognitive function, and functional studies of patient populations.[39–41] Following in the footsteps of functional MRI,[236,237] DOT is likely to play an important role in increasing our knowledge of brain activity associated with various stimulation paradigms, as well as our understanding of cerebral physiology, particularly the coupling between neuronal activity and the associated metabolic and vascular response. Interestingly, optical imaging is potentially the only neuroimaging modality that can measure the hemodynamic (see references above) and metabolic response[238–244] associated with neuronal activity, and measure neuronal activity directly.[245–247]

In the remainder of this section we describe three recent experiments. The first experiments measure flow, hemoglobin saturation, and hemoglobin concentration in a rat during stroke; this combination of parameters ultimately makes possible the assigment of oxygen metabolism changes to specific tissue volumes. The second and third sets of experiments image functional activation in the rat and in humans, with high spatial and temporal resolution.

21.4.3.1 Flow and Blood Oxygen Saturation Images of Rat Stroke

Experimenters at the University of Pennsylvania have used DOT to examine the spatial–temporal evolution of focal ischemia in a rat model.[248] Their measurements probe through the *intact* rat skull and combine "static" diffuse photon density wave measurements of Hb and HbO concentrations with "dynamic" diffuse correlation flowmetry (see Section 21.2.6). Their results are the first application of DOT correlation flowmetry to experimental stroke models.

Figure 21.16A shows the TTC stain of the infarct region of a focal ischemia induced in the rats by intraluminal suture occlusion of the middle cerebral artery. After 60 min of occlusion the suture was retracted for reperfusion. The animals recovered and, at 24 h after occlusion, were sacrificed for TTC staining. Differential images of the concentrations were reconstructed in a slice at a depth of 2 mm below the skull surface, extending 5 mm either side of midline and from 2 mm anterior of bregma to 8 mm posterior of bregma. The hemoglobin and flow images were obtained using the linear Rytov approach described in Sections 21.2.5.2 and 21.2.5.3.

Figure 21.16B shows image slices of total hemoglobin concentration ([HbT]), blood oxygen saturation StO$_2$, and relative changes in cerebral blood flow (rCBF) reconstructed with DOT. Note that the measurements cover the predominantly penumbral tissue and an equivalent tissue volume on the contralateral side. Image stacks were reconstructed from measurements averaged over five animals. Images are shown for time points representing baseline (−8 min), occlusion (+30 min), and reperfusion (+80 min). Regions of interest (ROIs) were defined for the contralateral and ipsilateral sides, consisting of 4 × 8 mm areas centered in the respective half of each image; the time traces for [Hb], StO$_2$, and (rCBF) in these regions are plotted in Figure 21.16C. Occlusion and saturation decreased by about 40% from baseline in the affected hemisphere. The numbers for flow are in reasonable agreement with near-surface laser Doppler measurements of penumbral tissues. The cerebral blood volume, on the other hand, showed much smaller percentage changes during occlusion.

These images demonstrate the feasibility of continuously imaging an integrated set of hemodynamic parameters through the time course of ischemia and reperfusion in experimental focal ischemia models. The combined measurements also offer the possibility to make quantitative maps of differential oxygen metabolism. A simplified model for oxygen metabolism relates two of the measurements made. If we assume that the product of the blood perfusion rate with the difference in oxyhemoglobin concentration between the artery perfusing the tissue and the vein draining the tissue equals the oxygen consumption rate, then the measured changes enable us to construct a map of local variations in cerebral oxygen metabolism in deep tissues.[197] This exciting prospect further enhances the attractiveness of the diffuse optical method.

21.4.3.2 Activation Imaging of Brain Function in a Rat Model

In this section we describe applications to functional activation of the rat brain. By using classical functional stimulation paradigms, these studies provide an opportunity to evaluate the imaging capabilities of diffuse optical tomography through comparisons with exposed cortex and fMRI studies.

These studies employed the CW system developed at the MGH-NMR center (see Section 21.3.1.1). The dual wavelength sources were positioned on a 3 × 3 grid interspersed within the 4 × 4 grid of detectors. In accordance with standard procedures used in exposed cortex studies of functional activation, the baseline hemoglobin concentrations were assumed — i.e., [Hb] = [HbO] = 50 μM.[249] Absorption coefficients were calculated using published spectra. The scattering coefficient was assumed to be equal to 10.0 cm^{-1}.

The experiments were performed on adult male Sprague-Dawley rats weighing 300 to 325 g. The rats were fasted overnight before measurements. The animals were anesthetized (Halothane 1 to 1.5%, N$_2$O 70%, O$_2$ 30%) and catheters were placed into a femoral artery to monitor the arterial blood pressure and into a femoral vein for drug delivery. The animals were tracheotomized, mechanically ventilated, and fixed on a stereotaxic frame. The probe was then placed symmetrically about midline. It covered a region from 2 mm anterior to 6 mm posterior of the rhinal fissure. After the surgical procedures,
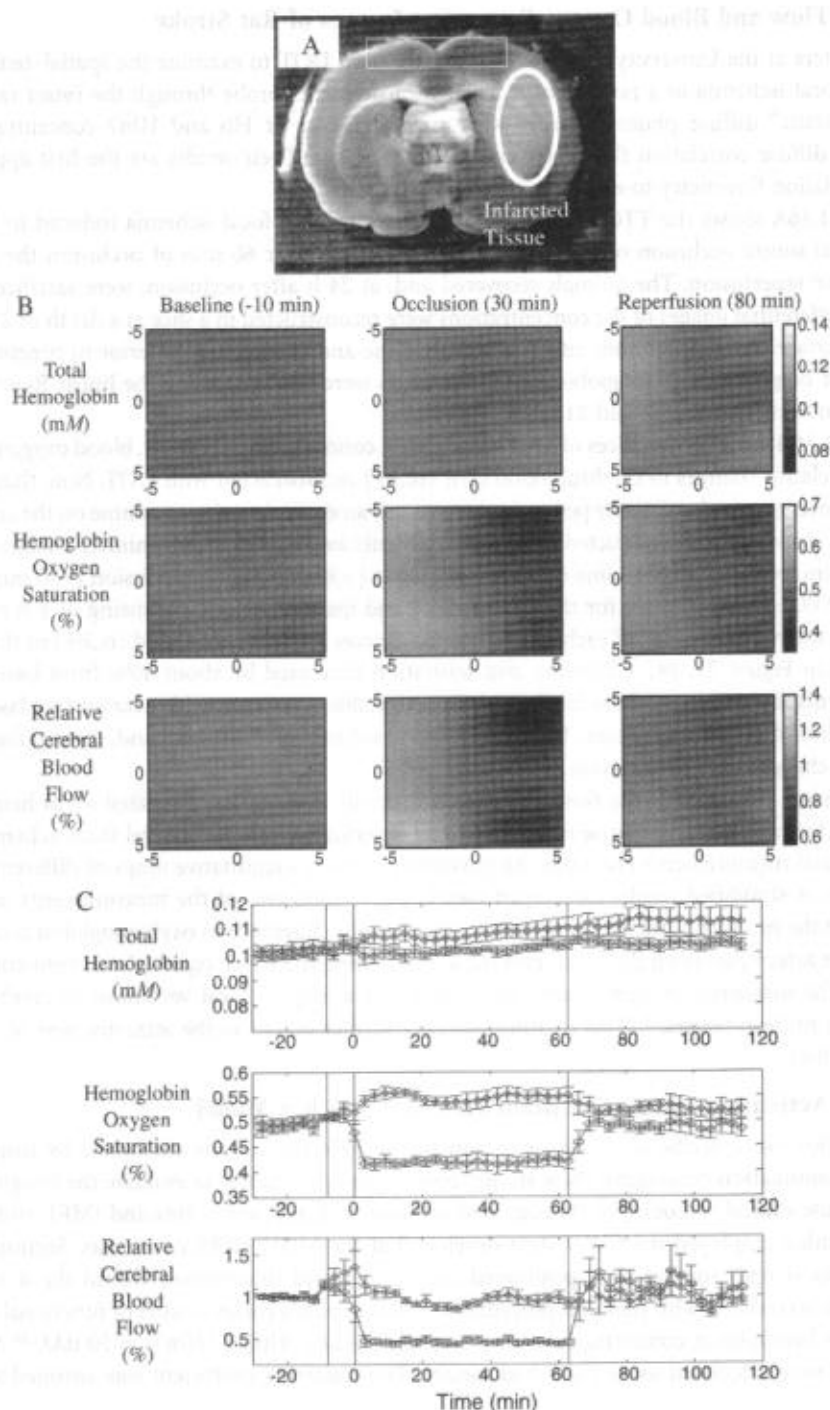
FIGURE 21.16 (A) TTC staining of infarct area; rectangle indicates slice position of DOT image reconstruction. (B–C) Diffuse optical tomography images of total hemoglobin concentrations, tissue averaged hemoglobin saturation, and relative cerebral blood flow (rCBF). A middle cerebral artery occlusion was performed during the time from $t = -5$ min to $t = 0$. The suture was retracted at $t = 60$ min resulting in reperfusion. (B) Images at baseline, during occlusion (+30 min) and +80 min. The spatial dimensions are given in millimeters. The scale bars indicate the concentration of hemoglobin, the percent oxygen saturation, and the relative blood flow change where 1 is no change and 1.4 is a 40% change. (C) The time traces for ipsilateral and contralateral ROIs.
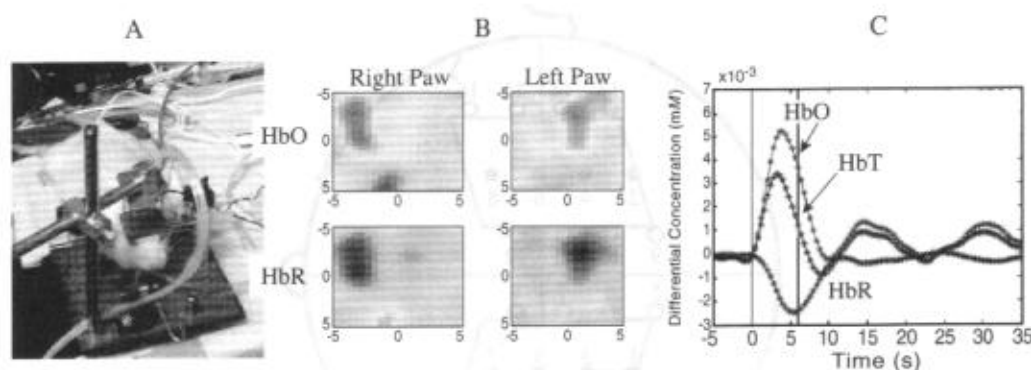
FIGURE 21.17 (A) Photograph of the DOT fibers on the rat scalp. (B) DOT images of oxy- and deoxyhemoglobin concentrations during functional activation of the somatosensory cortex. The oxyhemoglobin (HbO) images exhibit a concentration increase. The deoxyhemoglobin (HbR) images exhibit a concentration decrease. Images are shown for left- and right-forepaw stimulation, the activation showing up on the contralateral side. (C) Time-course of the hemoglobin concentration changes in the region of interest defined by the significant focal concentration change seen in (B).

Halothane was discontinued, and anesthesia was maintained with a 50 mg/kg intravenous bolus of α-chloralose followed by continuous intravenous infusion at 40 mg/kg/hr.

Electrical forepaw stimulation was performed using two subdermal needle electrodes inserted into the dorsal forepaw. The stimulus pattern was relayed to an isolated, pulsed current supply to provide 300 μ_s constant current pulses at programmed times. The current was maintained at 1.0 mA. A 3 Hz, 6-s stimulus was provided with 54-s interstimulus interval. The measurements were then averaged over 42 stimulus intervals. The final averaged temporal data stack was reconstructed frame by frame using the methods described in Sections 21.2.5.2 and 21.2.5.3. Each slice was reconstructed at a depth of 2 mm from the skull surface extending 5 mm either side of midline, and from 2 mm anterior of bregma to 8 mm posterior of bregma. The absorption image stacks were then converted to oxy- and deoxyhemoglobin image stacks.

The series of DOT [Hb] and [HbO] images show focal activation contralateral to the stimulated forepaw. The images are frames taken every 5 s. The time traces were extracted for a 3 × 3 mm area centered at maximal activation (see Figure 21.17). The oscillations seen after stimulus are similar to vasomotion signals seen by optical studies in exposed cortex.[250]

21.4.3.3 Images of Brain Function in Humans

The same MGH CW imaging system described in Section 21.3.2.1 was used to study 15 subjects during finger tapping, finger tactile stimulation, and median nerve electrical stimulation. The finger tapping and finger tactile protocols consisted of series of 10 stimulation/rest sequences for each hand (i.e., 20-s stimulation and 20-s rest), wherein the stimulation occurs at a frequency of ~4 to 5 Hz (the stimulus frequency of each subject was adjusted so as to be anharmonic with the heart rate). The median nerve electrical stimulation protocol consisted of a series of 18 stimulation/rest sequences (i.e., 10-s stimulation and 20-s rest) with stimulus intensity slightly above the motor threshold (i.e., using rectangular electrical pulses, current peak: <10 mA, duration: 0.2 ms, repetition rate: 4 to 5 Hz). Motion sensors were used on the fingers of the subjects to synchronize the stimuli with the optical signals recorded on the head.

The optical data were band-pass filtered between 0.02 to 0.50 Hz to correct for slow drifts and to reduce the ~1-Hz arterial pulsation amplitude. Finally, the multiple stimulation sequences were block averaged to achieve better statistics. This resulted in a time series of the measured signal intensity for each source-detector pair. Source-detector pairs near a region of brain activation showed changes similar to those seen in a rat as shown in Figure 21.18, while the other source-detector pairs showed little signal variation. Absorption images at the different wavelengths were converted into images of changes in oxy- and deoxyhemoglobin concentrations.
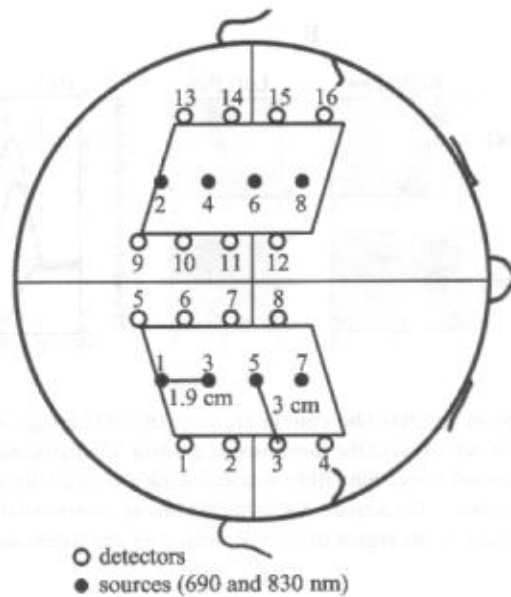
FIGURE 21.18 Geometrical arrangement of source and detector fibers on the head.

The hemodynamic response to stimulation was always visible in the optical data. During the finger tapping experiment, the oxy- and deoxyhemoglobin concentration variations were not sharply localized. This is probably because of a systemic elevation in blood volume, presumably resulting from a corresponding heart rate increase. During finger tactile stimulation, oxyhemoglobin increases were two to three times smaller than during finger tapping; also, oxy- and deoxyhemoglobin were sharply localized. During electrical stimulation, the hemoglobin changes were sharply localized and had a magnitude comparable with finger tactile stimulation. In the latter experiments a peculiar feature of ipsilateral decrease in blood volume was observed during the stimulation period (see Figure 21.19). By contrast, magnetoencephalography (MEG) and functional magnetic resonance imaging (fMRI) studies during median nerve stimulation have shown an activation of only the contralateral primary sensory-motor cortex.[251,252] A deactivation of the ipsilateral primary sensory-motor cortex has been observed in previous fMRI experiments during finger tapping;[255] these optical results suggest that a similar decrease in blood flow occurs in the ipsilateral cortex during electrical somatosensory stimulation.

In summary, DOT offers an exciting new method for studying human brain function, and should play an important role in the brain sciences when other imaging modalities (e.g., fMRI, EEG, MEG) are not attractive because of cost, sensitivity to motion artifacts, or confinement of the research subject.

21.5   Fundamental and Practical Issues: Problems and Solutions

In this final section we touch on some of the fundamental and practical difficulties associated with DOT. In particular, we discuss the fundamental limits of detection, characterization, and resolution, we discuss practical problems of source-detector calibration, and we briefly outline some of the ways researchers are overcoming these barriers.

21.5.1   Detection, Localization, Characterization, and Resolution Limits

The detection limits of DOT are set by the smallest signal perturbation that can be detected above the noise level. The spatial localization limit is generally the same as the detection limit because the maximum signal perturbation often occurs when an object is located directly between a source and detector. Full characterization of object optical properties, shape, size, and position is more difficult than detection and
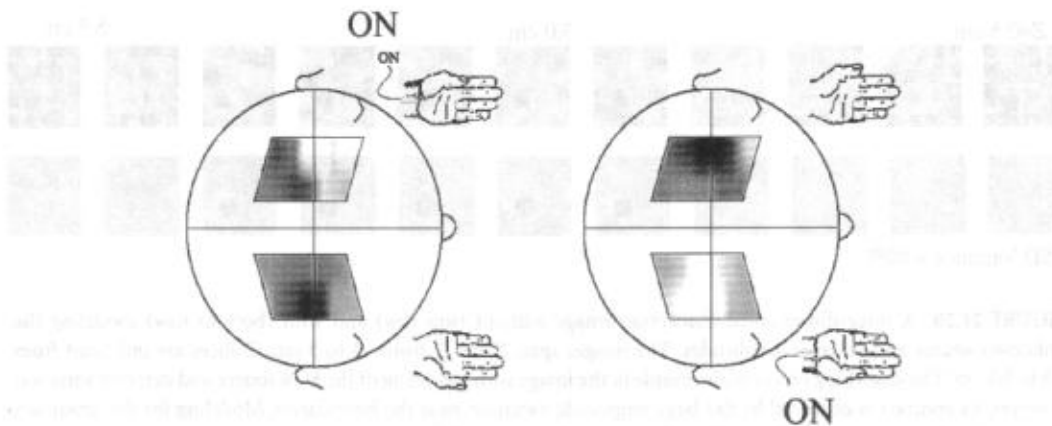
FIGURE 21.19 Block average hemoglobin maps at the end of the electrical stimulation period. Top panels: deoxy-hemoglobin changes; bottom panels: oxyhemoglobin changes. Left panels: left wrist median nerve stimulation; right panels: right wrist median nerve stimulation.

localization. For example, a fixed signal perturbation can be caused by a small, strongly absorbing object or a large, weakly absorbing object. The distinction between the large and small object must be derived from relative spatial differences in the perturbation of the measured fluence.

These limits have been extensively explored[254] for a transmission geometry applicable to breast imaging. In this work, a best-case scenario noise model assumed shot noise and small positional uncertainties gave rise to a random noise on the order of 0.1% of the signal intensity. Measurements were simulated in the transmission geometry with a single modulation frequency. With these assumptions about the noise, it was possible to detect 3-mm-diameter-absorbing objects that possessed a threefold greater absorption than the background. A similar analysis of the characterization limits indicated that simultaneous determination of object diameter and absorption coefficient required that object diameters were a minimum of 8 to 10 mm (for a 100% contrast); see Reference 254 for details. Another investigation,[255] focusing on resolution (defined as the FWHM of the fluence point-spread function caused by a localized perturbation,[255–257]) found that, if proper deconvolution of the measured data is performed, then resolutions of order 5 to 7 mm are possible with DOT.

There are potentially many ways to overcome some of these barriers, and many researchers are exploring the following possibilities, as well as other ideas. The brute force approach is to increase the number of measurements or decrease the measurement noise. This can be done, by increasing numbers of source-detector pairs, modulation frequencies, or optical wavelengths. The use of many optical wavelengths is beneficial because relatively few significant chromophores are in tissue and their spectra are well known. The use of prior spatial information, for example, the assignment of particular tissue types to specific volume elements of the image,[106,137,258] enables one to reduce the number of unknowns in the inverse problem and thus can effectively improve images. Optical techniques can also be combined with other imaging modalities (e.g., ultrasound[119,137,259] or MRI[13,260,261]) to constrain the DOT problem. Singular-value analysis of the tomographic weight matrix associated with specific data types, geometries, and optode arrangements has been developed recently[123] and should provide experimenters with quantitative tools to optimize for the spatial sampling interval, field-of-view parameters, resolution trade-offs, and, ultimately, physiology. Finally, it is now possible to reduce the systematic errors associated with source-detector amplitudes by directly incorporating these unknowns into the image reconstruction problem. This is the subject of the last section of this chapter.

21.5.2 Calibration of Source and Detector Amplitudes

The modeling of the DOT forward problem requires accurate knowledge of source and detector amplitudes and their positions. Systematic errors in the calibration of these parameters will result in absorption

Z=0.5 cm   3.0 cm   5.5 cm

SD Variance = 80%
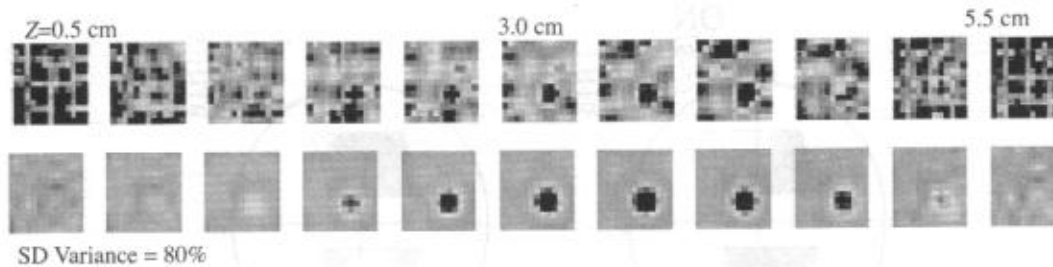
FIGURE 21.20 A three-dimensional absorption image without (top row) and with (bottom row) modeling the unknown source and detector amplitudes. The images span X and Y from -3 to 3 cm; Z-slices are indicated from 0.5 to 5.5 cm. The absorbing object is observable in the image with modeling of the 80% source and detector variance; however, its contrast is obscured by the large amplitude variation near the boundaries. Modeling for the unknown variance provides an image with significantly improved image quality.

and scattering image artifacts, e.g., image spikes near the positions of the sources and detectors. This type of artifact has been observed by a number of groups.[262] Some schemes to minimize these artifacts include median filtering[263] and spatial regularization; the latter approach penalizes the reconstruction near sources and detectors with a weight that varies exponentially from the sample surfaces.[113,262,264] The result is an image with suppressed variations near the sources and detectors, but with improved image quality further from the boundaries. However, the scheme has the undesirable effect of biasing the reconstruction away from the boundaries of the medium.

A recent and relatively simple solution to this problem models the uncertainties of source and detector amplitude and includes them in the inverse problem.[265] Within the linear Rytov approximation, the unknown source and detector amplitudes can be solved simultaneously with the unknown optical properties of the medium. We briefly outline this procedure next, assuming for simplicity a sample with absorption heterogeneities, but without scattering heterogeneities.

Recall the linear approximation for calculating fluence perturbations from spatial variation in the absorption and scattering coefficients, discussed in Section 21.2.5.2. The problem was written in the form $[W]\{x\} = \{b\}$ where $[W]$ represented the weight matrix, $\{x\}$ represented the unknown optical properties, and $\{b\}$ represented the difference between experiment and calculation (or the scattered wave). If we include the unknown source and detector amplitudes into the model, then the matrix equation can be reformulated as $[B]\{\xi\} = \{b\}$ where $[B] = [W'\ S\ D]$ and

$$\{\xi\} = \left\{ \frac{\delta\mu_{a,1}}{\mu_{ao}} \dots \frac{\delta\mu_{a,NV}}{\mu_{ao}} \ln s_1 \ \cdots \ \ln s_{NS} \ \ln d_1 \ \cdots \ \ln d_{ND} \right\}. \tag{21.22}$$

Here s_i and d_i represent the amplitude of the ith source and detector, respectively, NV is the number of voxels, NS is the number of sources, and ND is the number of detectors. Scaling $\delta\mu_{a,i}$ by μ_{ao} makes the elements dimensionless and of the same order as $\ln s$ and $\ln d$. $W' = \mu_{ao}W$ is the rescaling of the standard weight matrix. S and D are simple, well-defined matrices with block diagonal form that have 1 or 0 in the elements corresponding to particular sources and detectors.

Simulation results have demonstrated that incorporation of the unknown source and detector amplitudes into the inverse problem maintains image quality despite amplitude uncertainties greater than 50%. This is illustrated in Figure 21.20; a simulation of transmission through a 6-cm slab was considered with background optical properties of $\mu_{so}' = 10$ cm^{-1} and $\mu_{ao} = 0.05$ cm^{-1} and a 1.6-cm diameter absorbing sphere with $\mu_a = 0.15$ cm^{-1}, centered at $(x,y,z) = (1,1,3)$ cm. Measurements were made with 16 sources and 16 detectors equally spaced from -3 to 3 cm, and continuous-wave measurements were simulated. There was no additive measurement noise (i.e., shot or detector electronic noise) in the simulated data, only the multiplicative model error associated with the source and detector amplitudes.

Acknowledgments

References

1. Yodh, A. and Chance, B., Spectroscopy and imaging with diffusing light, *Phys. Today*, 48, 34, 1995.
2. Tromberg, B., Yodh, A., Sevick, E., and Pine, D., Diffusing photons in turbid media: introduction to the feature, *Appl. Opt.*, 36, 9, 1997.
3. Yodh, A., Tromberg, B., Sevick-Muraca, E., and Pine, D., Diffusing photons in turbid media, *J. Opt. Soc. Am. A*, 14, 136, 1997.
4. Boas, D.A., Brooks, D.H., Miller, E.L., DiMarzio, C.A., Kilmer, M., Gaudette, R.J., and Zhang, Q., Imaging the body with diffuse optical tomography, *IEEE Signal Process. Mag.*, 18, 57, 2001.
5. Miller, E., Focus issue: diffuse optical tomography — introduction, *Opt. Express*, 7, 461, 2000.
6. Chance, B., Near-infrared images using continuous, phase-modulated, and pulsed light with quantitation of blood and blood oxygenation, *Ann. N.Y. Acad. Sci.*, 838, 19, 1998.
7. Kang, K.A., Chance, B., Zhao, S., Srinivasan, S., Patterson, E., and Trouping, R., Breast tumor characterization using near-infrared spectroscopy, *Proc. SPIE*, 1888, 1993.
8. Suzuki, K., Yamashita, Y., Ohta, K., and Chance, B., Quantitative measurement of optical-parameters in the breast using time-resolved spectroscopy — phantom and preliminary *in-vivo* results, *Invest. Radiol.*, 29, 410, 1994.
9. Fishkin, J.B., Coquoz, O., Anderson, E.R., Brenner, M., and Tromberg, B., Frequency-domain photon migration measurements of normal and malignant tissue optical properties in a human subject, *Appl. Opt.*, 36, 10, 1997.
10. Grosenick, D., Wabnitz, H., Rinneberg, H.H., Moesta, K.T., and Schlag, P.M., Development of a time-domain optical mammograph and first *in vivo* applications, *Appl. Opt.*, 38, 2927, 1999.
11. Franceschini, M.A., Moesta, K.T., Fantini, S., Gaida, G., Gratton, E., Jess, H., Mantulin, W.W., Seeber, M., Schlag, P.M., and Kaschke, M., Frequency-domain techniques enhance optical mammography: initial clinical results, *Proc. Natl. Acad. Sci. U.S.A.*, 94, 6468, 1997.
12. Nioka, S., Miwa, M., Orel, S., Shnall, M., Haida, M., Zhao, S., and Chance, B., Optical imaging of human breast cancer, *Adv. Exp. Med. Biol.*, 361, 171, 1994.
13. Ntziachristos, V., Yodh, A.G., Schnall, M., and Chance, B., Concurrent MRI and diffuse optical tomography of breast after indocyanine green enhancement, *Proc. Natl. Acad. Sci. U.S.A.*, 97, 2767, 2000.
14. Cerussi, A.E., Berger, A.J., Bevilacqua, F., Shah, N., Jakubowski, D., Butler, J., Holcombe, R.F., and Tromberg, B.J., Sources of absorption and scattering contrast for near-infrared optical mammography, *Acad. Radiol.*, 8, 211, 2001.
15. Pogue, B.W., Poplack, S.P., McBride, T.O., Wells, W.A., Osterman, K.S., Osterberg, U.L., and Paulsen, K.D., Quantitative hemoglobin tomography with diffuse near-infrared spectroscopy: pilot results in the breast, *Radiology*, 218, 261, 2001.

16. McBride, T.O., Pogue, B.W., Gerety, E.D., Poplack, S.B., Osterberg, U.L., and Paulsen, K.D., Spectroscopic diffuse optical tomography for the quantitative assessment of hemoglobin concentration and oxygen saturation in breast tissue, *Appl. Opt.*, 38, 5480, 1999.

17. Delpy, D.T. and Cope, M., Quantification in tissue near-infrared spectroscopy, *Philos. Trans. R. Soc. London B*, 352, 649, 1997.

18. Painchaud, Y., Mailloux, A., Harvey, E., Verreault, S., Frechette, J., Gilbert, C., Vernon, M.L., and Beaudry, P., Multi-port time-domain laser mammography: results on solid phantom and volunteers, *Int. Symp. Biomed. Opt.*, 3597, 548, 1999.

19. Tromberg, B., Coquoz, O., Fishkin, J., Pham, T., Anderson, E.R., Butler, J., Cahn, M., Gross, J.D., Venugopalan, V., and Pham, D., Non-invasive measurements of breast tissue optical properties using frequency-domain photon migration, *Phil. Trans. R. Soc. London B*, 352, 661, 1997.

20. Sickles, E.A., Breast cancer detection with transillumination and mammography, *Am. J. Roentgenol.*, 142, 841, 1984.

21. Hoogenraad, J.H., van der Mark, M.B., Colak, S.B., Hooft, G.W., and van der Linden, E.S., First results from the Phillips Optical Mammoscope, in *Photon Propagation of Tissues III*, 31294, Benaron, D.A., Chance, B., and Ferrari, M., Eds., Plenum Press, New York, 1997, p. 184.

22. Ntziachristos, V., Ma, X.H., and Chance, B., Time-correlated single photon counting imager for simultaneous magnetic resonance and near-infrared mammography, *Rev. Sci. Instrum.*, 69, 4221, 1998.

23. Ntziachristos, V., Yodh, A.G., Schnall, M., and Chance, B., Comparison between intrinsic and extrinsic contrast for malignancy detection using NIR mammography, *Proc. SPIE*, 3597, 565, 1999.

24. Pogue, B.W., Poplack, S.D., McBride, T.O., Jiang, S., Osterberg, U.L., and Paulsen, K.D., Breast tissue and tumor hemoglobin and oxygen saturation imaging with multi-spectral near infrared computed tomography, in *Advances in Experimental Medicine and Biology Series*, Plenum Press, New York, 2001.

25. Pogue, B.W., Poplack, S.D., McBride, T.O., Jiang, S., Osterberg, U.L., and Paulsen, K.D., Near-infrared tomography: status of Dartmouth imaging studies and future directions, in progress.

26. Gopinath, S.P., Robertson, C.S., Grossman, R.G., and Chance, B., Near-infrared spectroscopic localization of intracranial hematomas, *J. Neurosurg.*, 79, 43, 1993.

27. Robertson, C.S., Gopinath, S.P., and Chance, B., A new application for near-infrared spectroscopy: detection of delayed intracranial hematomas after head injury, *J. Neurotrauma*, 12, 591, 1995.

28. Hintz, S.R., Cheong, W.F., Van Houten, J. P., Stevenson, D.K., and Benaron, D.A., Bedside imaging of intracranial hemorrhage in the neonate using light: comparison with ultrasound, computed tomography, and magnetic resonance imaging, *Pediatr. Res.*, 45, 54, 1999.

29. Hoshi, Y. and Tamura, M., Detection of dynamic changes in cerebral oxygenation coupled to neuronal function during mental work in man, *Neurosci. Lett.*, 150, 5, 1993.

30. Villringer, A., Planck, J., Hock, C., Schleinkofer, L., and Dirnagl, U., Near infrared spectroscopy (NIRS): a new tool to study hemodynamic changes during activation of brain function in human adults, *Neurosci. Lett.*, 154, 101, 1993.

31. Okada, F., Tokumitsu, Y., Hoshi, Y., and Tamura, M., Gender- and handedness-related differences of forebrain oxygenation and hemodynamics, *Brain Res.*, 601, 337, 1993.

32. Ruben, J., Wenzel, R., Obrig, H., Villringer, K., Bernarding, J., Hirth, C., Heekeren, H., Dirnagl, U., and Villringer, A., Haemoglobin oxygenation changes during visual stimulation in the occipital cortex, *Adv. Exp. Med. Biol.*, 428, 181, 1997.

33. Sakatani, K., Chen, S., Lichty, W., Zuo, H., and Wang, Y.P., Cerebral blood oxygenation changes induced by auditory stimulation in newborn infants measured by near infrared spectroscopy, *Early Hum. Dev.*, 55, 229, 1999.

34. Obrig, H., Wolf, T., Doge, C., Hulsing, J.J., Dirnagl, U., and Villringer, A., Cerebral oxygenation changes during motor and somatosensory stimulation in humans, as measured by near-infrared spectroscopy, *Adv. Exp. Med. Biol.*, 388, 219, 1996.